CrossMark

J. Fluid Mech. (2015), *vol.* 784, *pp.* 252–273. © Cambridge University Press 2015
doi:10.1017/jfm.2015.564

Effects of three-dimensionality on instability and turbulence in a frontal zone

Eric Arobone[1] **and Sutanu Sarkar**[1],†

[1]Department of Mechanical and Aerospace Engineering, University of California San Diego, CA 92093, USA

(Received 1 December 2014; revised 23 July 2015; accepted 22 September 2015; first published online 4 November 2015)

Linear stability analysis and direct numerical simulation are used to investigate the evolution of a symmetrically unstable uniform frontal zone. Simulations in a three-dimensional computational domain capable of resolving near-symmetric currents develop strong nonlinearities without the emergence of pure symmetric instability. Linear stability analysis demonstrates that for $ft > 1$ (f is the Coriolis parameter and t denotes time) the flow generates strongly asymmetric structures which become nearly symmetric when $ft \gg 1$. Unlike the currents generated during pure symmetric instability, near-symmetric instability generates currents that do not align with isopycnals. This greatly modifies their energetics and evolution, leading to regions of the flow that are unstable to gravitational instability and energized by the reservoir of available potential energy. A high-resolution simulation demonstrates the flow evolution from near-symmetric currents to secondary shear-convective instabilities and finally, through tertiary instabilities, to fully three-dimensional turbulence. The effect of this sequence of instabilities is quantified through velocity and vorticity statistics as well as budgets for turbulent kinetic and potential energy. It is not until $ft \sim 10$ that the energy source for fluctuations is primarily shear, in contrast to the purely symmetric instability which draws its energy exclusively from shear production.

Key words: ocean processes, stratified turbulence, turbulent flows

1. Introduction

The symmetric instability (SI) is an instability of baroclinic zonal flows where perturbations contain no longitudinal variation, and are thus two-dimensional. The baroclinic zonal flow model (Eady 1949), a fundamental geophysical flow problem that is discussed by Pedlosky (1987), takes the form of a sheared flow $u(z)$ that balances a density field of the form $\rho(y, z)$ in a rotating frame. Here, $N^2 = -(g/\rho_0)\partial\rho/\partial x_3$ is the buoyancy frequency, f is the Coriolis parameter and $S^2 = (\|\partial \boldsymbol{u}_h/\partial x_3\|)^2$ is the squared vertical shear of horizontal velocity components. Also, x, y, z or x_1, x_2, x_3 are used to denote streamwise, spanwise and vertical coordinates. The symmetric instability dominates the instability of the Eady flow when the Richardson number ($Ri = N^2/S^2$) is between 0.25 and 0.95, while baroclinic and

† Email address for correspondence: ssarkar@ucsd.edu

https://doi.org/10.1017/jfm.2015.564 Published online by Cambridge University Press

Kelvin–Helmholtz (K–H) instabilities dominate at higher and lower Ri respectively, as shown by Stone (1966). In a more general case that includes relative vorticity ω_i due to horizontal shear ($\partial u/\partial y$), instability is manifested when the potential vorticity (PV, $q = -\rho_0^{-1}(\omega_i + f\delta_{i3})\partial\rho/\partial x_i$) is of opposite sign to the Coriolis parameter in stably stratified regions, as noted in Hoskins (1974). These more general flows are susceptible to inertial/centrifugal and symmetric instabilities which act on the absolute vertical vorticity opposing planetary rotation and vertical shear respectively. In general, balanced baroclinic zonal flows have PV given by $q = -fS^2 + (\omega_3 + f)N^2$ (Thomas *et al.* 2013). Therefore, since $S^2 = M^4/f^2$ for a balanced zonal flow with $M^2 = -(g/\rho_0)\partial\rho/\partial x_2$, the PV may take the opposite sign of f for a sufficiently strong front with large cross-front buoyancy gradient, M^2.

An exceptionally sharp (1 km) front near the beginning of the Kuroshio extension was investigated by D'Asaro *et al.* (2011). Shipboard measurements, a Lagrangian float and a towed profiling vehicle allowed for measurements of the turbulence intensity (inferred from vertical motions of the float), temperature, salinity, pressure and velocity profiles. The front is less than 1 km wide and approximately 20 m deep, and contains vertical motion resulting from upper-ocean turbulence. Dissipation at the front is estimated to be 10–20 times stronger than outside the front, but surface winds and cooling are too weak to explain the observed turbulence. The PV was found to take the opposite sign of f for 0.2 days while the vessel passed through the front, strongly suggesting symmetric instability as the relevant mechanism. These results imply that in some regions of the upper ocean, lateral density gradients and symmetric instability may be more important than atmospheric forcing in setting the turbulence intensity.

The evolution of a symmetrically unstable density frontal zone is examined using linear stability theory and two-dimensional nonlinear numerical simulations in Taylor & Ferrari (2009). The *a priori* assumption of symmetric instability (no along-front or x_1 variation in figure 1), also adopted in previous numerical studies of the problem by Thorpe & Rotunno (1989) and Griffiths (2003*a*,*b*), allowed Taylor & Ferrari (2009) to employ the two-dimensional (x_2, x_3) approximation for the flow. Linear stability analysis demonstrated that for large $|N/f|$, viscous effects on the slopes of the symmetric currents are negligible and that $Ri < 0.25$ is satisfied locally before the symmetric currents become fully nonlinear. Once the instability reaches finite amplitude, a secondary K–H instability forms. Following the secondary instability, small-scale turbulence entrains positive PV into the mixed layer from the thermocline, resulting in a rapid equilibration of the flow as the PV approaches zero throughout the mixed layer.

Instabilities in a baroclinic zonal flow are explored in Molemaker, McWilliams & Capet (2010) using quasigeostrophic and Boussinesq nonlinear simulations. This study explores the emergence of a forward energy cascade in a flow with $Ro = |S/f| < 1$ but not $Ro \ll 1$, with $Ri = N^2/S^2 > 1$. The domain size is too small to observe the baroclinic instability, while Ri is too large for symmetric instability. Turbulence in the Boussinesq case emerges via the generation of sharp fronts (locally $Ri < 1$ and $Ro > 1$) and subsequent frontal instabilities in the interior of the flow. Unbalanced motions represent only a small portion of the total kinetic energy of the flow, yet they are essential in driving energy to dissipative scales. The results suggest that total energy lost during spin-down of the flow approaches a constant value for the Boussinesq cases while approaching zero for quasigeostrophic cases as $Re \to \infty$. The inference is that frontal instabilities could play an important role in the extraction of energy from largely balanced flows, even far away from ocean boundaries.

https://doi.org/10.1017/jfm.2015.564 Published online by Cambridge University Press

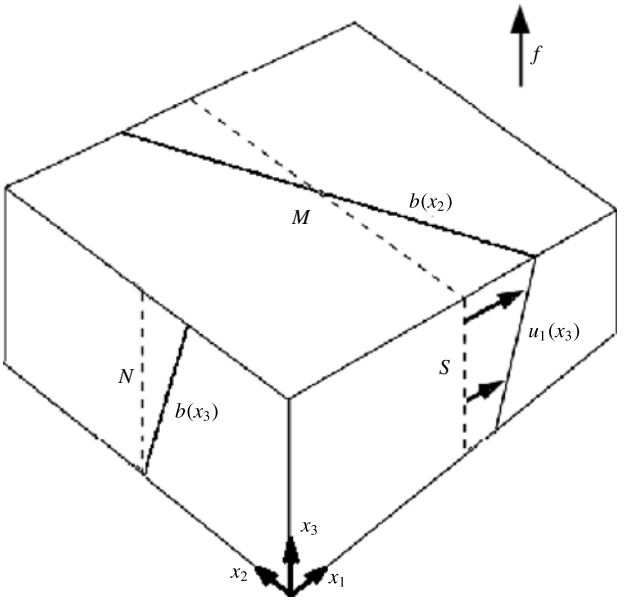


FIGURE 1. Schematic showing a stratified vertically sheared flow, $u_1(x_3)$, in thermal wind balance representing a small subsection of a stably stratified frontal zone. Spatial gradients in velocity and buoyancy are shown along with their respective time scales. Here, $M^2 = \partial b/\partial x_2$, $N^2 = \partial b/\partial x_3$ and $S = \partial u_1/\partial x_3$. The along-front direction is x_1 and the lateral (spanwise) direction is x_2.

The stability analysis of Stone (1966) is greatly expanded in Stone (1970) to include the parameter regime where perturbations are not nearly aligned with the spanwise (x_2) or longitudinal (x_1) direction. The growth rates of tilted modes depend only on the tilt angle magnitude, and not its direction. Additionally, the strongest growth rates never occur in the newly explored regime, instead occurring near the configuration of baroclinic ($k_2 = 0$) or symmetric ($k_1 = 0$) instability, depending on Ri.

The three-dimensional counterpart ($k_1 \neq 0$) to symmetric instability is explored in greater detail in Jones & Thorpe (1992) using non-hydrostatic numerical simulation. The basic flow is two-dimensional with velocity given by $u_1(x_3)$ and $\rho(x_2, x_3)$, such that $|S/f| = 50$ and $Ri = 0.4$. The linear evolution is explored with respect to three initially symmetric perturbation types: a streamfunction perturbation isolated in the x_2 direction, a density perturbation isolated in the x_2 direction and a density perturbation isolated in the x_2 and x_3 directions (parcel perturbation). Initially, the first and second perturbation types lose symmetry, developing a counterclockwise angle of horizontal tilt relative to the symmetric axis, resulting in decreased $\langle u_2' u_3' \rangle$, slowing perturbation growth. Later, both perturbations rotate in a clockwise manner, reducing tilt and increasing growth. The parcel perturbation leads to tilting only in the clockwise direction. Analysis showed that asymmetric modes (also called non-symmetric modes) with $k_1 \neq 0$ grow fastest for large perturbation length scales, while symmetric modes grow fastest for small-scale disturbances.

The asymptotic ($t \to \infty$) behaviour of asymmetric ($k_1 \neq 0$) modes is of interest. Lott, Plougonven & Vanneste (2012) have shown that hydrostatic perturbations with $k_1 \neq 0$ are stable. The more general case of non-hydrostatic perturbations has been studied recently by Salhi & Pieri (2014), who show that the homogeneous Eady flow

https://doi.org/10.1017/jfm.2015.564 Published online by Cambridge University Press

is neutrally stable to asymmetric fluctuations at long time. However, transient growth due to the non-normal nature of the linear operators in homogeneous constant shear flow may lead to appreciable growth of a variety of initial perturbations. Indeed, Mamatsashvili *et al.* (2010) show that even though symmetric modes dominate as $t \to \infty$, there exists the possibility for non-symmetric modes to be favoured over finite time scales when $Ri < 1$ and $Ro = |S/f| \geqslant 1$. Optimal growth was determined for $Ri = 0.3$, 0.6 and 0.9 and $Ro = 1$, 3 and 10 over the characteristic time period associated with symmetric instability ($T = \sigma^{-1} \sim O(f^{-1})$). In the three $Ro = 10$ cases, the energy gained by the optimal non-symmetric mode was over ten times greater than the growth in the symmetric mode. In all simulated cases, the optimal growth occurred when modes were significantly asymmetric with $-1.84k_2 < k_1 < -0.48k_2$. Salhi & Pieri (2014) formulated the transient growth problem for linearized disturbances in the unbounded problem using a decomposition into toroidal, poloidal and buoyancy modes. Substantial amplification in the energy of asymmetric modes was obtained for $Ri < 1$ and $Ro > 1$ during the transient growth stage until the perturbations equilibrated to constant-amplitude inertia-gravity waves.

Direct numerical simulations of a zonal baroclinic flow were performed by Pieri *et al.* (2013). Here, Ri and M^2/N^2 were varied extensively and their effects on homogeneous turbulence identified. Turbulence grows in the symmetrically unstable range only when $M^2/N^2 > 0.2$. For $Ri \sim 0.1$, the PV distributions are rather symmetric but the asymmetry increases with increasing Ri, with the asymmetry being in favour of negative PV. The results were from simulations at a fairly low microscale Reynolds number with $Re_{\lambda,0} = 33$, and simulations were performed over short time intervals ($0 < St < 20$) such that development of SI was limited.

The present study is an investigation of the sequence of frontal instabilities and the path to turbulence in a symmetrically unstable flow with $Ri = 0.5$. We are interested in the consequences of allowing full three-dimensionality of fluctuations on both linear instabilities and nonlinear evolution into turbulence. The dependence of the nature of the primary instability on the along-front domain size is explored in § 3, demonstrating that there is strong transient growth of asymmetric modes for all cases and that there is a shift of the long-time perturbation flow from symmetric currents to near-symmetric currents as the horizontal domain size increases. Non-modal linear stability analysis is used in § 4 to explain the behaviour of the flow perturbations prior to secondary instabilities, in order to understand the growth of asymmetric modes and the change of asymmetry with increasing time. The properties of asymmetrically growing modes are explored in § 5 using simulations of horizontally tilted structures in both two- and three-dimensional flow; here, the domain is rotated horizontally about the z axis to preferentially yield currents aligned with the grid and to improve the resolution of the horizontally tilted structures. Lastly, a scaled-down version of the front is used in § 6 to explore the progression from asymmetric currents to secondary instabilities to turbulence, explaining the vorticity dynamics and quantifying the turbulence energetics. For instance, the evolution of the three components of fluctuating vorticity in figure 14 shows the imprint of secondary instability and tertiary instability through which the initially linearly evolving primary instability transitions to three-dimensional turbulence.

2. Formulation

The dimensional equations for conservation of mass, momentum and density for a Boussinesq fluid in a frame of reference rotating about the vertical axis are given

https://doi.org/10.1017/jfm.2015.564 Published online by Cambridge University Press

below with dimensional variables denoted by *. Centrifugal acceleration is included as a centrifugal potential and included within the pressure gradient.

$$\left.\begin{gathered}\frac{\partial u_i^*}{\partial x_i^*}=0,\\ \frac{\partial u_i^*}{\partial t^*}+\frac{\partial (u_i^* u_j^*)}{\partial x_j^*}+\epsilon_{i3k} f^* u_k^* = -\frac{1}{\rho_0^*}\frac{\partial p^*}{\partial x_i^*}-\frac{\rho'^* g^*}{\rho_0^*}\delta_{i3}+\nu^*\frac{\partial^2 u_i^*}{\partial x_j^* \partial x_j^*},\\ \frac{\partial \rho^*}{\partial t^*}+\frac{\partial (\rho^* u_j^*)}{\partial x_j^*}=\kappa^*\frac{\partial^2 \rho^*}{\partial x_j^* \partial x_j^*}.\end{gathered}\right\} \tag{2.1}$$

The density and pressure fields are decomposed in the following manner:

$$\left.\begin{gathered}\rho^*(x_i^*, t^*)=\rho_0^*+\frac{\partial \bar{\rho}^*}{\partial x_2^*}x_2^*+\frac{\partial \bar{\rho}^*}{\partial x_3^*}x_3^*+\rho'^*(x_i^*, t^*),\\ p^*(x_i^*, t^*)=\overline{p}^*(x_2^*, x_3^*)+p'^*(x_i^*, t^*),\end{gathered}\right\} \tag{2.2}$$

where $\overline{\rho}^*$ represents the background stratification and $\overline{p}^*$ is in hydrostatic and geostrophic balance with the initial density profile $(\rho_0^*+\overline{\rho}^*)$ and initial mean velocity profile respectively. The initial mean velocity corresponds to uniform vertical shear of the form

$$f^*\frac{\partial \bar{u}_1^*}{\partial x_3^*}=\frac{g^*}{\rho_0^*}\frac{\partial \bar{\rho}^*}{\partial x_2^*}. \tag{2.3}$$

Additionally, we introduce variables $M^{*2}=-g^*/\rho_0^*\times \partial\bar{\rho}^*/\partial x_2^*$ and $N^{*2}=-g^*/\rho_0^*\times \partial\bar{\rho}^*/\partial x_3^*$, where $g^*>0$ is the magnitude of gravitational acceleration. The vertical shear is $S^*=-M^{*2}/f^*$ due to geostrophic balance. It should be noted that $M^{*2}<0$ in the present problem because $\partial\bar{\rho}^*/\partial x_2^*$ is taken to be positive. The physical problem of interest is illustrated in figure 1, corresponding to zooming in on a strong submesoscale front. For case L1_64, the physical domain (L_1^*, L_2^*, L_3^*) corresponds to a region that is approximately 640 m (along front) $\times$ 80 m (lateral) $\times$ 10 m (vertical). The non-dimensional variables for this problem are given as

$$t=|M^*|t^*,\quad x_i=\frac{x_i^*}{L_3^*},\quad u_i=\frac{u_i^*}{|M^*|L_3^*},\quad \rho'=\frac{-\rho'^*}{L_3^*(\partial\overline{\rho}^*/\partial x_2^*)},\quad p'=\frac{p'^*}{\rho_0^*|M^{*2}|L_3^{*2}}. \tag{2.4a–e}$$

The following non-dimensional equations for mass conservation, momentum conservation and density perturbation evolution are obtained along with relevant non-dimensional parameters:

$$\frac{\partial u_i}{\partial x_i}=0, \tag{2.5}$$

$$\frac{\partial u_i}{\partial t}+\frac{\partial (u_i u_j)}{\partial x_j}+\epsilon_{i3k} f u_k=-\frac{\partial p'}{\partial x_i}+Ekf\frac{\partial^2 u_i}{\partial x_j \partial x_j}-\rho'\delta_{i3}, \tag{2.6}$$

$$\frac{\partial \rho'}{\partial t}+\frac{\partial (\rho' u_j)}{\partial x_j}+u_2-\beta u_3=\frac{Ekf}{Pr}\frac{\partial^2 \rho'}{\partial x_j \partial x_j}, \tag{2.7}$$

$$Ek=\frac{\nu^*}{f^* L_3^{*2}},\quad f=\frac{f^*}{|M^*|},\quad \beta=\frac{N^{*2}}{|M^{*2}|},\quad Pr=\frac{\nu^*}{\kappa^*}. \tag{2.8a–d}$$

https://doi.org/10.1017/jfm.2015.564 Published online by Cambridge University Press

Case	Ek	θ (deg.)	f	β	L_1	L_2	L_3	N_1	N_2	N_3
L1_4	10^{-4}	0	0.152	21.4	4	8	1	64	256	128
L1_8	10^{-4}	0	0.152	21.4	8	8	1	128	256	128
L1_16	10^{-4}	0	0.152	21.4	16	8	1	256	256	128
L1_32	10^{-4}	0	0.152	21.4	32	8	1	512	256	128
L1_64	10^{-4}	0	0.152	21.4	64	8	1	1024	256	128
L1_128	10^{-4}	0	0.152	21.4	128	8	1	2048	256	128
2D0	10^{-4}	0	0.152	21.4	0	8	1	1	1024	128
2D5	10^{-4}	5	0.152	21.4	0	8	1	1	1024	128
2D10	10^{-4}	10	0.152	21.4	0	8	1	1	1024	128
3D0	2×10^{-4}	0	0.152	21.4	8	8	1	256–1024	256–1024	128
3D5	2×10^{-4}	5	0.152	21.4	8	8	1	256–1024	256–1024	128
3D10	2×10^{-4}	10	0.152	21.4	8	8	1	256–1024	256–1024	128
Turb10	2×10^{-4}	10	0.25	8	4	4	1	256–1024	256–1024	256

TABLE 1. Simulation parameters and case names. Here, L_i and N_i represent the length of the domain and the number of computational points respectively in each direction. The Richardson number in all cases is $Ri = f^2\beta = 0.5$ and $Pr = 1$. Multiple grids are used in simulating the bottom four cases to increase the resolution as the flow becomes progressively more nonlinear.

Based on these non-dimensional parameters the Richardson number for the base flow is given by $Ri = f^2\beta$ and the Rossby number based on vertical shear is $Ro = f^{-2}$. Our interest is in the evolution of geophysical flows in frontal regions, i.e., $f \ll 1$ and $\beta \gg 1$, while $Ri = f^2\beta < 1$ and $Ro = f^{-2} > 1$. In particular, we will take $Ri = 0.5$ and perform several simulations, as summarized in table 1. A Reynolds number, Re, can be defined based on the streamwise velocity difference, U^*, across the channel height, L_3^*, and the molecular viscosity, ν^*. The value of $Re = U^*L_3^*/\nu^* = 1/(f^2\,Ek)$ is 80 000 for case Turb10 which resolves the fine-scale three-dimensional turbulence resulting from the breakdown of instabilities, and is somewhat larger for the other 3D and 2D cases which are continued only to the stage of primary and secondary instabilities.

The flow evolves in a horizontally periodic channel of height L_3^* with free-slip walls. Homogeneous Neumann boundary conditions are used for u_1, u_2 and ρ' at $z = 0$ and $z = 1$, providing free-slip and no perturbation mass flux conditions at vertical boundaries. Homogeneous Dirichlet boundary conditions are used to constrain $u_3 = 0$ at the upper and lower boundaries. The pressure deviation from the hydrostatic geostrophic background satisfies $\partial p'/\partial n = 0$ at the upper and lower boundaries. Periodicity is enforced in both horizontal directions for the variables u_1, u_2, u_3, ρ' and p'.

3. Effect of domain size

This study begins with three-dimensional simulations in the same parameter regime as the two-dimensional simulations of Taylor & Ferrari (2009). Initially, there is a rapid growth of three-dimensional asymmetric modes, but, later in time, the degree of asymmetry decreases. By systematically changing the streamwise domain length, L_1, we will also show that the dominant instability mode that eventually emerges retains some asymmetry in the case of large L_1. The initial conditions contain three-dimensional fluctuations in addition to uniform shear and buoyancy gradients. The initial fluctuations are small, containing approximately 10^{-6} times the total energy

https://doi.org/10.1017/jfm.2015.564 Published online by Cambridge University Press

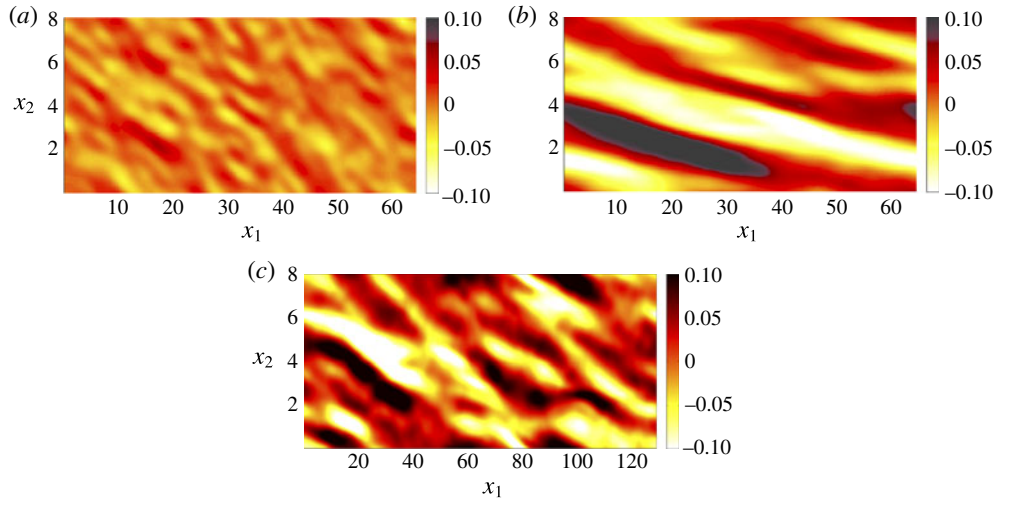


FIGURE 2. (Colour online) Contours of vertical vorticity (ω_3) from case L1_64 when (*a*) $t = 2.17f^{-1}$ and (*b*) $t = 7.09f^{-1}$ along with case L1_128 when (*c*) $t = 5.43f^{-1}$. The cases with smaller L_1 two-dimensionalize (i.e. energy contained primarily in $k_1 = 0$ modes) well before $t \sim 7f^{-1}$. Both (*b*) and (*c*) were taken immediately preceding the development of strong nonlinearity.

contained in the uniform shear. The numerical algorithm uses either second-order central differencing or sixth-order compact differencing on a grid that is staggered in the x_2 and x_3 directions. An in-house parallelized multigrid Poisson solver is used to solve for the pressure deviation, p', from the initial balanced pressure every Runge–Kutta substep using either second- or fourth-order finite difference stencils and red–black Jacobi or Gauss–Seidel smoothing. The Navier–Stokes and density equations are evolved using a third-order Runge–Kutta time-marching scheme. Parallelization is accomplished using a message passing interface (MPI). Case-specific computational details are shown in table 1. The two-dimensional simulations use a kinetic energy spectrum of $E \propto k^8 \exp(-4k^2/k_0^2)$, while the three-dimensional cases include only those modes where $10k_h^2 \leqslant k_3^2$ using a spectrum of the form $E \propto k^4 \exp(-2k^2/k_0^2)$. The restriction is introduced to prevent energy from going into large-k_1 modes which are rapidly dissipated in the three-dimensional cases.

Due to the fact that the dependence on the along-front domain length (L_1) is not known *a priori*, a range of horizontal aspect ratios ($0.5 \leqslant L_1/L_2 \leqslant 16$) were used. In all simulations varying L_1, the vertical vorticity quickly organized into structures aligned primarily along the horizontal axis tilted approximately 45° asymmetric in the clockwise direction, as illustrated by figure 2(*a*). The emergence of asymmetric modes for moderate *ft* values is consistent with Mamatsashvili *et al.* (2010). As time progressed, the vertical vorticity gradually reduced its degree of asymmetry and increased in horizontal scale, as seen in figure 2(*b*). The reduction of asymmetry of the fluctuation modes with increasing time in the simulations is consistent with the linear analysis result of Salhi & Pieri (2014) that asymmetric fluctuations are asymptotically stable as $t \to \infty$. In all L1_ cases except L1_64 and L1_128 the flow rapidly two-dimensionalizes to purely symmetric ($k_1 = 0$) fluctuations before the development of strong nonlinearity. The time associated with two-dimensionalization

https://doi.org/10.1017/jfm.2015.564 Published online by Cambridge University Press

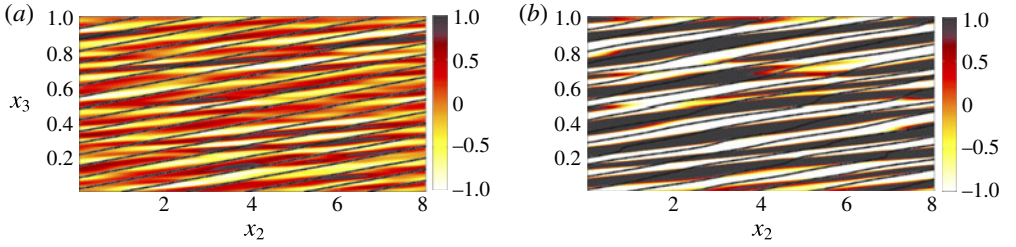


FIGURE 3. (Colour online) Contours of along-front vorticity (ω_1) and isopycnals from case L1_64 when (*a*) $t = 2.17f^{-1}$ and (*b*) $t = 7.09f^{-1}$. The cases with L_1 smaller than 64 display far greater alignment between ω_1 and isopycnals when $t \sim 7f^{-1}$.

increases with increasing L_1, until cases L1_64 and L1_128, which develop strong nonlinearities before the flow can reach a symmetric state. For structures with a lateral width of δ, periodicity implies that the smallest asymmetric angle possible is $\theta \sim \tan^{-1}(\delta/L_1)$, indicating that the capture of modes with a small degree of asymmetry requires $L_1 \gg \delta$.

The misalignment of ω_1 structures (asymmetric instability currents) with respect to isopycnals throughout the simulation is seen in figure 3. The misalignment becomes less dramatic at later time as the flow becomes more nonlinear and the vortical structure aligns more with the symmetric axis. The reason why large L_1 is needed to capture near-symmetry is due to the periodic boundary conditions in the x_1 direction and the large horizontal scale (k_h^{-1}) of the instability modes. When L_1 is not sufficiently large (e.g. the L1_4, L1_8 and L1_16 cases), then energy rapidly transfers from the $\theta \sim \tan^{-1}(\delta/L_1)$ currents to symmetric ($\theta = 0$) currents rather than θ continuing to decrease gradually as in the L1_64 and L1_128 cases. Expanding the analysis of Mamatsashvili *et al.* (2010), § 4 seeks to further explain the evolution of asymmetric flows towards near- as opposed to purely symmetric modes. In the 3D5 and 3D10 cases, the computational domain is rotated about the vertical axis to reduce the L_1 required to capture currents with a small degree of asymmetry.

4. Linear stability analysis

Linear stability analysis is employed to understand the evolution of asymmetry of the fluctuations that was described in § 3. Mamatsashvili *et al.* (2010) explored the early transients ($t \sim f^{-1}$), but we are more interested in longer evolution times since secondary instability occurs when $t \gg f^{-1}$ in this flow. The base state corresponding to a balanced uniform front is given by

$$\langle u_1 \rangle = Sx_3 = -\frac{M^2}{f}x_3, \quad \langle \rho \rangle = \rho_0 + \nabla_2(\langle \rho \rangle)x_2 + \nabla_3(\langle \rho \rangle)x_3. \tag{4.1a,b}$$

Assuming modes of the form $\phi(t)\exp(\mathrm{i}k_j x_j)$, one finds that $\mathrm{d}k_3/\mathrm{d}t = M^2 k_1/f$ as a direct consequence of flow homogeneity. Assuming positive S and f it follows that M^2 must be negative. Rotating the domain about the vertical axis such that $\tan\theta = k_1/k_2$ allows for new coordinates such that $\tilde{k}_1 = 0$ and $\tilde{k}_2 = k_h$. Under this transformation the symmetric instability corresponds to $\theta = 0$, allowing exploration of the effect of

https://doi.org/10.1017/jfm.2015.564 Published online by Cambridge University Press

asymmetry by varying θ. The following linear inviscid governing equations describe motion in the rotated coordinate system:

$$\left.\begin{gathered}\frac{\mathrm{d}u_1'}{\mathrm{d}t} = fu_2' + \cos\theta\frac{M^2}{f}u_3', \quad \frac{\mathrm{d}u_2'}{\mathrm{d}t} = -fu_1' - \sin\theta\frac{M^2}{f}u_3' - \mathrm{i}k_h p'/\rho_0, \\ \frac{\mathrm{d}u_3'}{\mathrm{d}t} = -\mathrm{i}k_3 p'/\rho_0 - g\rho'/\rho_0, \quad \frac{\mathrm{d}\rho'}{\mathrm{d}t} = -\sin\theta\frac{\partial\langle\rho\rangle}{\partial x_2}u_1' - \cos\theta\frac{\partial\langle\rho\rangle}{\partial x_2}u_2' - \frac{\partial\langle\rho\rangle}{\partial x_3}u_3', \\ 0 = \mathrm{i}k_h u_2' + \mathrm{i}k_3 u_3'.\end{gathered}\right\} \tag{4.2}$$

From continuity, the pressure and vertical velocity variables can be expressed as functions of the other variables. Introducing the buoyancy $b' = -g\rho'/\rho_0$, temporarily normalizing all wavenumber components with respect to $\|\boldsymbol{k}\|$, and introducing the wavevector angle ϕ defined by $\tan\phi = k_h/k_3$ gives the following perturbation evolution equation of the form $\mathrm{d}\phi_i'/\mathrm{d}t = A_{ij}\phi_j'$:

$$\frac{\mathrm{d}}{\mathrm{d}t}\begin{bmatrix}u_1'\\u_2'\\b'\end{bmatrix} = \begin{bmatrix}0 & (f - \cos\theta\tan\phi M^2/f) & 0\\ -f\cos^2\phi & \sin\theta\sin\phi\cos\phi M^2/f & -\sin\phi\cos\phi\\ -\sin\theta M^2 & \tan\phi N^2 - \cos\theta M^2 & 0\end{bmatrix}\begin{bmatrix}u_1'\\u_2'\\b'\end{bmatrix}. \tag{4.3}$$

The sin terms above grow in influence as the modes become more asymmetric. Taking $\theta = 0$, or for purely symmetric instability, and assuming modes of the form $\exp(\mathrm{i}k_j x_j + \sigma t)$ one obtains a characteristic equation of the form

$$\sigma^2 = \cos^2\phi[M^4/N^2 - f^2 - N^2(\tan\phi - M^2/N^2)], \tag{4.4}$$

agreeing with the relation given in Taylor & Ferrari (2009) for geophysical modes ($\cos\phi \approx 1$). As N/f increases the range of unstable current slopes (k_2/k_3) decreases, peaking at the isopycnal slope.

Reverting back to non-normalized wavenumbers, it is worth noting that $k_3(t)$ evolves with time, k_1 and k_2 remain fixed at their initial values, and the wavenumber magnitude, $k(t)$, also evolves with time. The time evolutions of the vertical wavenumber (Moffatt 1967; Rogallo 1981) and wavenumber norm are given as

$$\frac{\mathrm{d}k_3}{\mathrm{d}t} = -Sk_1 = \frac{M^2}{f}k_1 \quad \text{and} \quad \frac{\mathrm{d}k}{\mathrm{d}t} = \frac{M^2}{f}\frac{k_1 k_3}{k}. \tag{4.5a,b}$$

This implies that the frontal strength, degree of asymmetry and initial alignment of the wavenumber affect how rapidly shear modifies k_3/k and the underlying mechanism of instability. The non-modal stability problem is solved through introduction of

$$\left.\begin{gathered}\boldsymbol{E}_{ij}^2(t) = \delta_{ij} + \delta_{i2}\delta_{2j}k_h^2 k_3^{-2}(t), \quad \boldsymbol{D}(t) = \left(\frac{\mathrm{d}\boldsymbol{E}(t)}{\mathrm{d}t} + \boldsymbol{E}(t)\boldsymbol{A}(t)\right)\boldsymbol{E}^{-1}(t) \\ \text{and } \boldsymbol{\Phi}(T) = \exp\left(\int_0^T \boldsymbol{D}(t)\,\mathrm{d}t\right).\end{gathered}\right\} \tag{4.6}$$

The perturbation energy is given by $\|\boldsymbol{D}(t)\boldsymbol{\phi}(t)\|^2$ and the perturbation energy growth over period T is given by the square of the maximum real eigenvalue of $\boldsymbol{\Phi}(T)$.

Figure 4 shows the results of the stability analysis, namely the eigenvalues of $\boldsymbol{\Phi}(T)$ normalized by f for SI with $Ri = 0.5$, for which one finds $\sigma = f$. As time increases, a trend of gradually decreasing asymmetry (the black band of high growth rates shifts

https://doi.org/10.1017/jfm.2015.564 Published online by Cambridge University Press

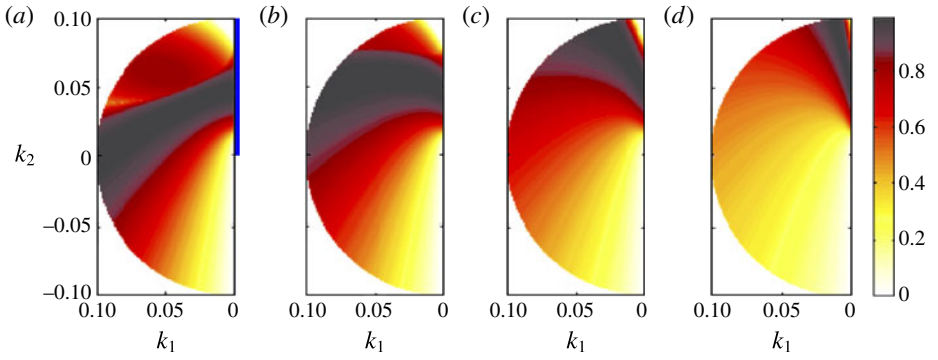


FIGURE 4. (Colour online) Plots showing the maximum real eigenvalues (normalized by f) corresponding to the system of equations $\mathrm{d}\phi_i'/\mathrm{d}t = A_{ij}\phi_j'$. Growth rates for $Ri = 0.5$ are shown over various periods given by $T = f^{-1}$ (*a*), $2f^{-1}$ (*b*), $4f^{-1}$ (*c*) and $8f^{-1}$ (*d*). Here, non-dimensional parameters match the regime explored in simulations L1_64 and L1_128. The wavenumber components k_1 and k_2 have been normalized by $\|\boldsymbol{k}\|$ here and $k_3 < 0$ initially. The dark vertical line in (*a*) indicates the symmetric axis.

towards $k_1 = 0$) is found, agreeing with the results of § 3. In these plots it is assumed that $k_3 < 0$, but changing the sign of k_3 simply mirrors the results about the symmetric axis. It should be noted that modes with $k_3 < 0$ and $k_1 > 0$ have

$$\frac{\mathrm{d}k_3^2}{\mathrm{d}t} = \frac{2M^2}{f}k_1k_3 > 0, \tag{4.7}$$

since $M^2 < 0$. Thus, the magnitude of k_3/k_2 progressively increases and the velocity (perpendicular to the wavenumber) of the associated instability currents becomes more horizontal.

It is difficult to generate purely symmetric instability when three-dimensional perturbations are allowed because of the stabilization of modes with $k_1 < 0$ (right half-plane, not shown in figure 4) by strong stratification. For small negative k_1, the stabilization of near-symmetric modes is dramatic, with $\mathrm{d}k_3/\mathrm{d}t = -Sk_1 \propto -\sin\theta$ implying a change of sign in $\mathrm{d}k_3/\mathrm{d}t$ about the symmetric axis. The wavenumbers of these modes, initially with $k_3 < 0$ and $\theta < 0$, have $\mathrm{d}k_3/\mathrm{d}t > 0$ and $\mathrm{d}k_3^2/\mathrm{d}t < 0$ so that, with increasing time, the magnitude of k_3/k_2 progressively decreases and the associated currents become more vertical. Once these currents become more vertical than isopycnals in the frontal zone they are rapidly stabilized by background stratification. Thus, it is not surprising that it is difficult to generate purely symmetric modes in the limit of $L_1/L_2 \gg 1$ (e.g. the L1_64 and L1_128 simulations) given that the symmetric axis is nearly the stability boundary for small $|f|$ and large $\beta = N^2/|M^2|$. Decreasing $|f|$ increases the rate at which currents with $k_1 < 0$ become more vertically oriented, while increasing β increases the stratification strength.

As f is decreased at fixed Ri, the stability diagrams do not change appreciably other than modification of the horizontal scale due to change in β. Reducing Ri to 0.3 results in modes that are less asymmetric, but the general trend in figure 4 is still found. Three-dimensional fluctuations grow at nearly or greater than the symmetric growth rate throughout the range of time scales associated with the development of SI when the strict requirement of $k_1 = 0$ is relaxed. Nevertheless, it is because of

https://doi.org/10.1017/jfm.2015.564 Published online by Cambridge University Press

the tendency for currents to become more aligned with the symmetric axis as time increases that we shift our attention to understanding the development of secondary shear instabilities in symmetric and nearly symmetric flows.

5. Effect of asymmetry

The preceding sections on three-dimensional simulations and linear stability analysis show that fluctuations at late time can take the form of asymmetric modes; the symmetric mode with $\theta = 0$ is a special case. Therefore, we further study numerically the influence of non-zero but small θ on the nonlinear evolution of the flow.

5.1. *Two-dimensional simulations*

Several two-dimensional simulations were performed in a rotated coordinate system before proceeding to three-dimensional simulations. The first simulation mimicked that of Taylor & Ferrari (2009) with identical f, β and Ek. The other two simulations are identical except that the computational domain is rotated counterclockwise about the vertical axis by 5° in case 2D5 and 10° in case 2D10 (i.e. $\theta = 5°$ and $\theta = 10°$). This is similar to the rotation of the linear modes in the previous section. In the linear stability analysis, solutions were constant along planes of the form $k_i x_i = C$ and therefore were one-dimensional, varying only in the direction of $\boldsymbol{k}$. These nonlinear two-dimensional simulations allow for fluctuations that are constant along horizontal lines of the form $k_1 x_1 + k_2 x_2 = C$, where $k_1 = \tan\theta k_2$. Throughout this and the following sections it is assumed that x_1 and x_2 are in the rotated domain, unless otherwise stated. Due to our interest in nearly symmetric modes (small θ) the distinction should be minor.

The non-modal stability analysis of § 4 and simulations L1_64 and L1_128 illustrate the tendency for large-scale currents to nearly but not exactly align with the symmetric axis when $t \gg f^{-1}$. Based on the observation that case L1_64 becomes strongly nonlinear when structures are 5° asymmetric, one can compare the two-dimensional symmetric instability growth of perturbations with the asymmetric growth observed in L1_64 and the tilted two-dimensional simulation with $\theta = 5°$. Figure 5 shows that the growth of fluctuations in case L1_64 agrees better with the asymmetric two-dimensional simulation (2D5) than the symmetric simulations (2D0 and T&F) after the initial flow adjustment. The reduction in growth relative to the 2D0 case is primarily due to vertical shearing of the asymmetric instability, because the growth rate associated with infinitesimal time (maximal real eigenvalue of $\boldsymbol{A}$ from § 4) only reduces to 99.3 % of the symmetric value. The fluctuations initially decay in the two-dimensional simulations in contrast to the three-dimensional cases due to the fact that the three-dimensional instabilities of Mamatsashvili *et al.* (2010) associated with growth over $T \sim f^{-1}$ (similarly demonstrated in figure 4) cannot be manifested in the two-dimensional nearly symmetric cases.

Snapshots of isopycnals and plane-normal vorticity from the symmetric (2D0) and $\theta = 10°$ (2D10) cases are displayed in figure 6 as the flow becomes nonlinear. The primary distinctions between $\theta = 0$ and $\theta = 10°$ are due to the linear prediction of (4.5). In the asymmetric case, the initial mean shear has a vorticity component in the rotated x_1 coordinate ($\langle\omega_1\rangle = \partial\langle u_2\rangle/\partial x_3 = -M^2 \sin\theta/f = 1.14$) which continually reduces the vertical inclination of currents, giving rise to currents that are shallower than isopycnals. The increase of $|k_3|$ by vertical shearing suggests that the vertical length scale, $\delta = 2\pi/k_3$, in the asymmetric cases should be lower than in the symmetric case, but this is not observed because of viscous effects. The viscous growth rate for SI with $Ri = 0.5$ is given by

$$\sigma/f \sim \sqrt{Ri^{-1} - 1} - 4\pi^2 Ek/\delta^2. \tag{5.1}$$

https://doi.org/10.1017/jfm.2015.564 Published online by Cambridge University Press

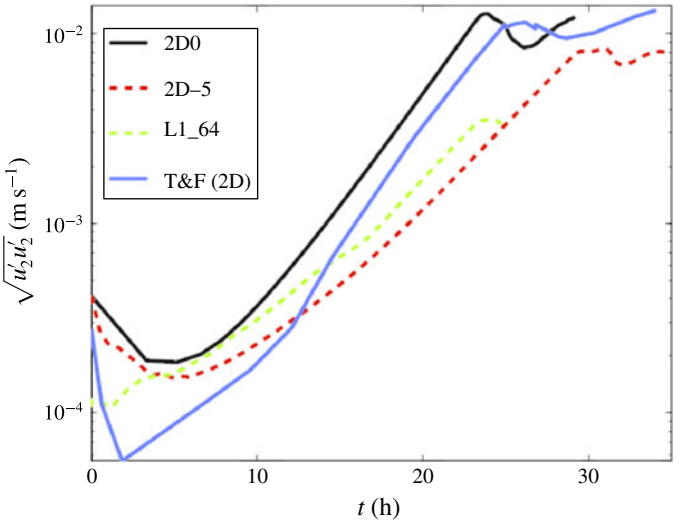


FIGURE 5. (Colour online) Evolution of across-front fluctuations in two-dimensional simulations with varying tilt and a three-dimensional simulation (L1_64) with no tilt and a large along-front domain length. Values from Taylor & Ferrari (2009) (blue curve) were obtained by digitizing a linear plot, and therefore values are unreliable for $\sqrt{u_2'u_2'} < 10^{-3}$ m s^{-1}.

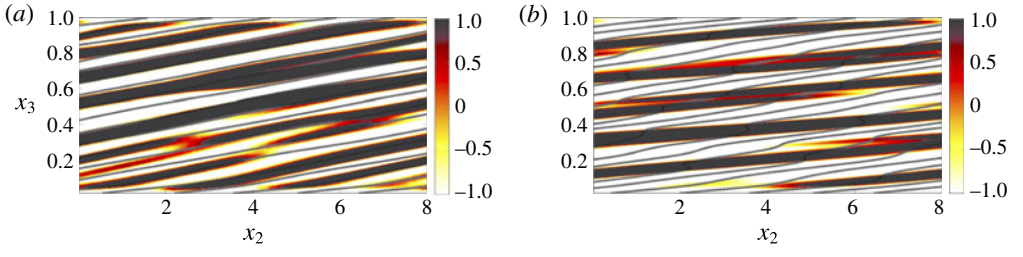


FIGURE 6. (Colour online) Contours of ω_1 from two-dimensional simulations where (*a*) $\theta = 0°$ and $t = 6.84f^{-1}$ and (*b*) $\theta = 10°$ and $t = 13.4f^{-1}$. Isopycnals are also shown by thin solid curves.

This implies that the growth rates should rapidly drop off (for instance, decrease by more than 25 %) when the vertical scale is $\delta \lesssim 1/8$ for $Ri = 0.5$ and $Ek = 10^{-4}$. The continual shearing due to non-zero $\langle\omega_1\rangle$ leads to merging of currents and misalignment with respect to isopycnals, but shearing does not reduce the vertical scale of currents due to currents forming at a scale already marginally influenced by viscosity.

The fluctuation kinetic energy budgets are shown for cases 2D0 and 2D10 in figures 7(*a*) and 7(*b*) respectively. The terms contained in the budgets are

$$P = -\langle u_i'u_j'\rangle \frac{\partial\langle u_i\rangle}{\partial x_j}, \quad B = -\langle u_3'\rho'\rangle \quad \text{and} \quad \epsilon = 2Ek\langle s_{ij}'s_{ij}'\rangle. \tag{5.2a–c}$$

Here, P is the shear production, B is the buoyancy flux and ϵ is the viscous dissipation. It takes considerably longer to develop asymmetric currents, as anticipated from the

https://doi.org/10.1017/jfm.2015.564 Published online by Cambridge University Press

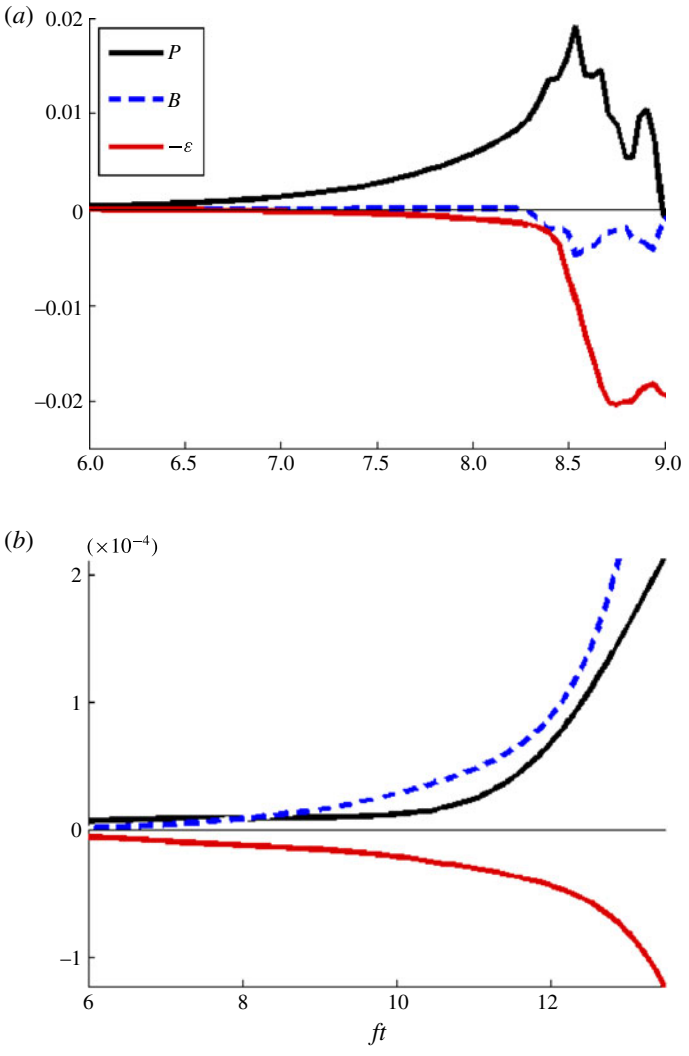


FIGURE 7. (Colour online) Volume-averaged turbulent kinetic energy budgets from two-dimensional simulations with (*a*) $\theta = 0°$ and (*b*) $\theta = 10°$. The difference in magnitudes between cases is due to exponential growth in the symmetric case, while growth is slower in the $\theta = 10°$ case due to the non-modal nature of instability.

non-modal linear stability analysis for $ft \gg 1$. Buoyancy flux plays a dramatically different role in the two cases, only contributing as a sink after the symmetric case breaks down and being a significant energy source for the asymmetric case.

5.2. *Three-dimensional simulations*

In cases 3D0, 3D5 and 3D10 the spatial extent in the x_1 direction is set to 8, allowing for increased spatial resolution relative to the L1_64 and L1_128 cases at comparable computational cost. This reduced domain size allows for increased resolution of the secondary K–H instability that was first explored in the two-dimensional simulations of Taylor & Ferrari (2009). In two-dimensional simulations K–H rollers are forced

https://doi.org/10.1017/jfm.2015.564 Published online by Cambridge University Press

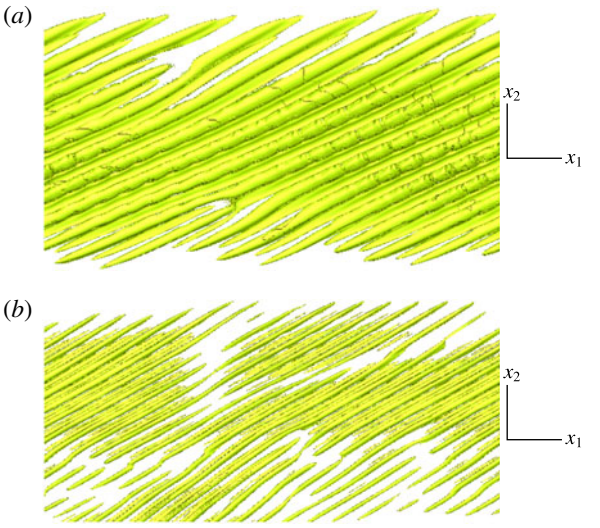


FIGURE 8. (Colour online) Isosurface of λ_2 during the development of secondary instability for (*a*) case 3D0 when $t = 9.08f^{-1}$ and (*b*) case 3D10 when $t = 7.93f^{-1}$.

to align with the x_1 direction, unlike in the three-dimensional simulations. Figure 8 shows λ_2 isocontours (Jeong & Hussain 1995) capturing coherent vortical structures emerging as a result of secondary K–H instability whose orientation is substantially tilted with respect to the x_1 axis. The emergence of the K–H rollers is most rapid in the symmetric cases, while the wavelength associated with instability decreases as the asymmetry increases. The faster growth rates associated with SI are responsible for the more rapid emergence of localized regions with $Ri < 0.25$ in the 3D0 case. In figure 9 the development of secondary shear instability is shown for cases 3D0 and 3D10 through vertical slices of ω_1. A slight difference is observed between the slopes of the instability currents, with the 3D10 case yielding shallower slopes than the 3D0 case, as expected.

The coherent secondary K–H rollers are inclined with respect to the x_1 axis, as explained by the following analysis. For symmetric instability ($k_h/k_3 = \beta^{-1}$ and $\theta = 0$) the modal stability problem simplifies to an eigenvalue problem of the form $\lambda_{max}\boldsymbol{\phi} = \boldsymbol{A\phi}$ with $b' = 0$. Solving for the corresponding eigenvector gives

$$\begin{bmatrix} u_1' \\ u_2' \\ u_3' \end{bmatrix} = \begin{bmatrix} \sqrt{(Ri^{-1} - 1)(1 + \beta^{-2})} \\ -1 \\ \beta^{-1} \end{bmatrix} \exp\left(\mathrm{i}\beta^{-1}k_3x_2 + \mathrm{i}k_3x_3 + k_3\sqrt{Ri^{-1} - 1}ft\right), \quad (5.3)$$

which predicts that SI currents will flow at a horizontal angle significantly tilted with respect to the symmetric axis. In the case of $Ri = 0.5$ and $\beta^{-2} \ll 1$, it follows that $u_1' = -u_2'$, i.e. an angle of 45° is predicted. Cases 3D0, 3D5 and 3D10 were not able to resolve the intense nonlinearity observed after breakdown of the secondary instability. Section 6 will explore the transition to turbulence of a similar ($Ri = 0.5$) front investigated in case Turb10.

https://doi.org/10.1017/jfm.2015.564 Published online by Cambridge University Press

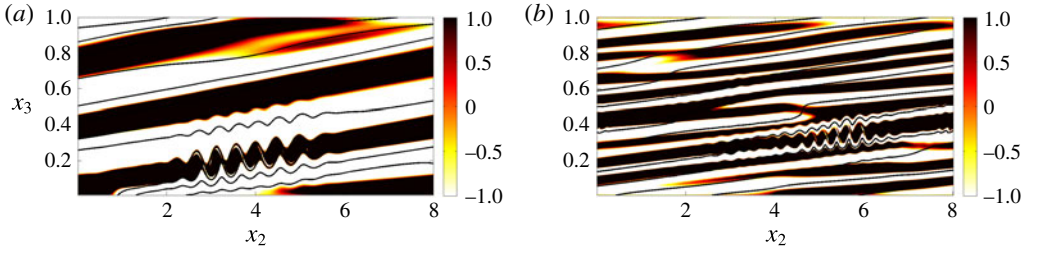


FIGURE 9. (Colour online) Contours of ω_1 from three-dimensional simulations showing the development of secondary instabilities where (*a*) $\theta = 0°$ and $t = 8.98f^{-1}$ and (*b*) $\theta = 10°$ and $t = 8.67f^{-1}$. Isopycnals are also shown by thin solid curves.

6. Frontal turbulence

A three-step process drives the transition from linearly evolving perturbations to turbulence in this flow. The three steps, indicated in figure 14, correspond to secondary instability, tertiary instability and finally three-dimensional turbulence. Before an expanded discussion in §§ 6.1 and 6.2, we provide the following summary of the transition process. During the first step (approximately $ft < 9$), the off-SI currents grow in a manner consistent with the linear stability analysis. These modes correspond to vortex sheets that are not aligned with isopycnals and contain primarily ω_1'. The vortex sheets become unstable to secondary shear-convective instability at $ft \sim 9$. Early during the secondary instability, ω_2' is small and has little to no x_1 dependence. As the secondary instability progresses, the vortex sheets become nonlinear, rapidly rolling up and generating horizontal vorticity fluctuations, increasing both $\omega_1'^2$ and $\omega_2'^2$. Both components increase due to the asymmetric orientation of coherent vortices during the secondary instability. The secondary instability results in the generation of some vertical vorticity fluctuations. However, the mean shear, $S = \partial u_1/\partial x_3$, of the balanced flow is stable with respect to ω_2 fluctuations for $Ri = 0.5$, and it is not until the organization in the x_1–x_3 plane is disrupted through tertiary instabilities, commencing at $ft \sim 11$, that the flow starts to transition to three-dimensional turbulence with significantly large levels of all three components of vorticity fluctuation.

Computational exploration of turbulence in a strong submesoscale front using direct numerical simulation is challenging due largely to the wide range of time scales ($S^* \sim N^* \gg |M^*| \gg f^*$) influencing flow evolution. By increasing $f = f^*/|M^*|$ from 0.152 to 0.25 and decreasing $\beta = N^{*2}/|M^{*2}|$ from 21.4 to 8 in case Turb10, we are able to reduce S/f by a factor of almost three without significantly violating the separation of time scales implicit at frontal regions. Increasing the grid resolution by a factor of two is additionally helpful to fully resolve the secondary shear-convective instabilities which will be discussed in this section. In order to reduce the computational complexity, the size of the domain in each of the horizontal directions is reduced by a factor of two to focus on turbulence rather than merely the evolution of the nearly symmetric currents. In this section, x_1 and x_2 correspond to coordinates in the domain rotated about the vertical axis such that x_1 is aligned with the near-symmetric currents. The angle of rotation is taken to be $\theta = 10°$, which is close to the orientation of the primary vortical modes that appeared in lower-resolution three-dimensional simulations.

https://doi.org/10.1017/jfm.2015.564 Published online by Cambridge University Press

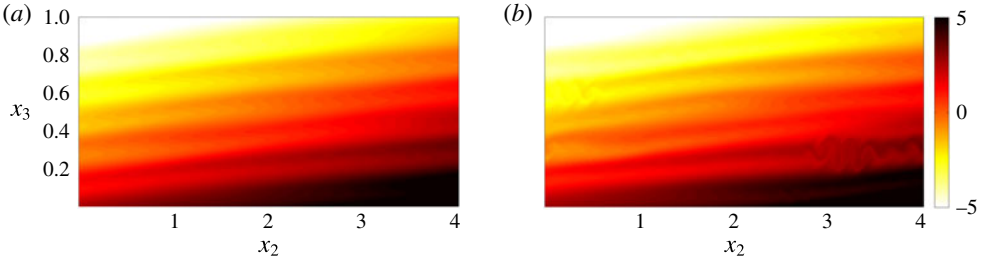


FIGURE 10. (Colour online) Vertical snapshots of density variation ($\rho - \rho_0 = \rho' + x_2 - \beta x_3$) in case Turb10 when $t = 9f^{-1}$ (a) and $t = 9.23f^{-1}$ (b) showing density fluctuations immediately preceding and during secondary instability.

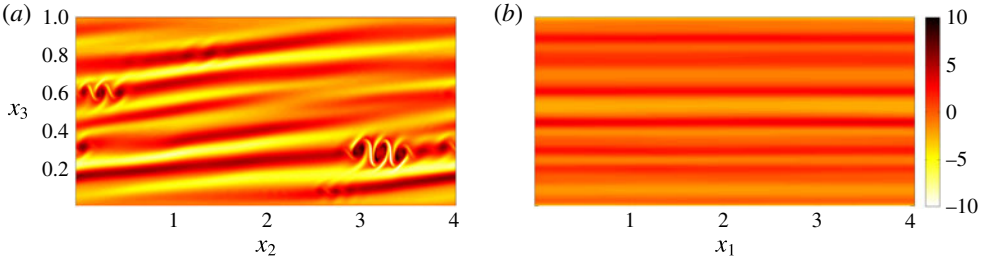


FIGURE 11. (Colour online) A vertical plane of ω_1 from case Turb10 at $x_1 = 2$ (a) and a vertical plane of ω_2 at $x_2 = 2$ (b) showing horizontal vorticity in case Turb10 during secondary instability at $t = 9.15f^{-1}$.

6.1. *Qualitative features*

The two distinct features of off-SI not observed in SI are the misalignment of currents and isopycnals and the fact that buoyancy flux is a significant source of fluctuating kinetic energy. These two features are related in the sense that vertical shear drives misalignment which then drives motion across isopycnals, leading to a density variation very similar to that seen in the Turb10 case in figure 10. Unstably stratified regions appear throughout the domain as a result of these slantwise currents. Eventually the shear and unstable density anomaly grow strong enough to lead to secondary instability. The vorticity signature associated with the development of secondary instability (the resulting coherent structures were visualized in figure 8) is shown in figure 11. At this time the two-dimensional assumption appears reasonable, with ω_2 in the x_1–x_3 plane showing nearly no dependence on x_1. The regions of the density field being strongly stirred in figure 10 coincide with vortex sheets with positive vorticity in figure 11. After this point (i.e. $ft > 9$), the secondary instability exhibits weak variability in the x_1 direction.

Eventually, the variability in ω_2 fluctuations grows sufficiently strong to rapidly destabilize the vertical vorticity field. Figure 12 shows the development of tertiary shear instability once the ω_2 fluctuations are strong enough to meander and extract energy from the vertical shear. Prior to this point ($ft < 10.7$), the mean vorticity, $\langle\omega_2\rangle = \partial\langle u_1\rangle/\partial x_3$, of the original balanced flow was strong relative to the ω_2 fluctuations. The secondary shear-convective instability is required to rapidly increase ω_2 fluctuations, because the quasi-two-dimensional near-SI currents of the primary instability do not effectively augment ω_2'. The flow rapidly three-dimensionalizes after

https://doi.org/10.1017/jfm.2015.564 Published online by Cambridge University Press

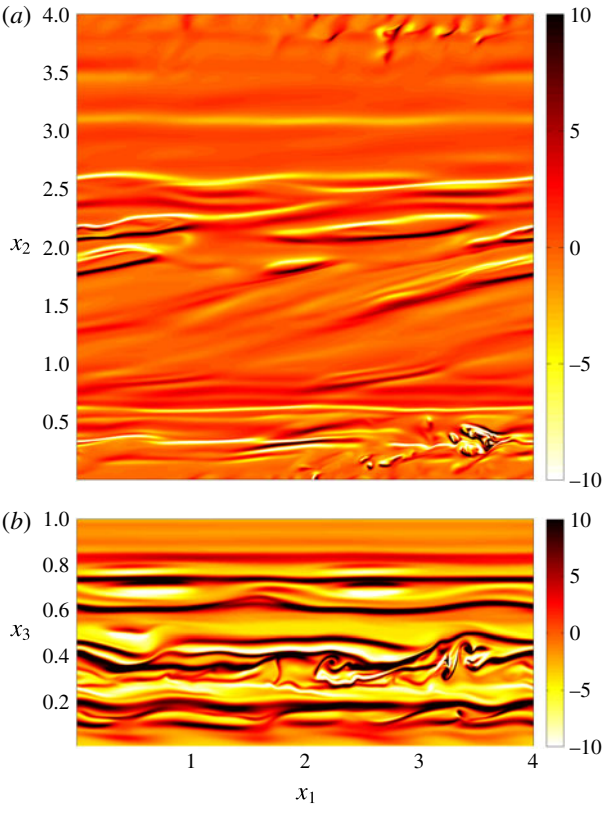


FIGURE 12. (Colour online) A vertical plane of ω_2 from case Turb10 at $x_2 = 2$ (b) and a horizontal plane of ω_3 at $x_3 = 0.5$ (a) when $t = 10.7f^{-1}$. Snapshots of horizontal and vertical vorticity are shown when the flow begins to three-dimensionalize.

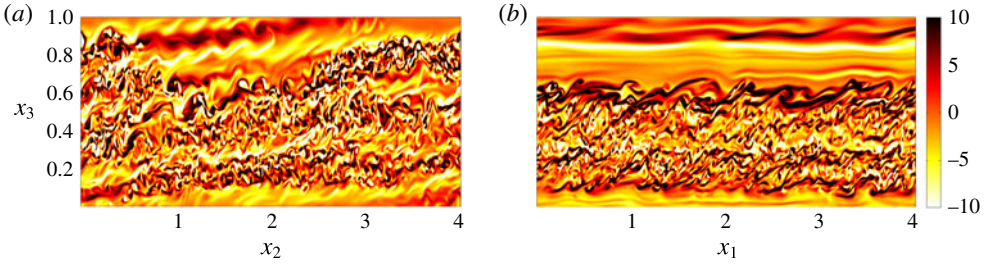


FIGURE 13. (Colour online) A vertical plane of ω_1 from case Turb10 at $x_1 = 2$ (a) and a vertical plane of ω_2 with $x_2 = 2$ (b) at $t = 11.6f^{-1}$. Snapshots of horizontal vorticity are taken when strong turbulence fills most of the domain.

the manifestation of the tertiary instability, destabilizing the balanced flow in the strongly sheared x_1–x_3 plane. Figure 13 shows ω_1 and ω_2 vorticity fluctuations as the domain rapidly fills with turbulence. By the end of the simulation, nearly the whole computational domain appears turbulent.

https://doi.org/10.1017/jfm.2015.564 Published online by Cambridge University Press

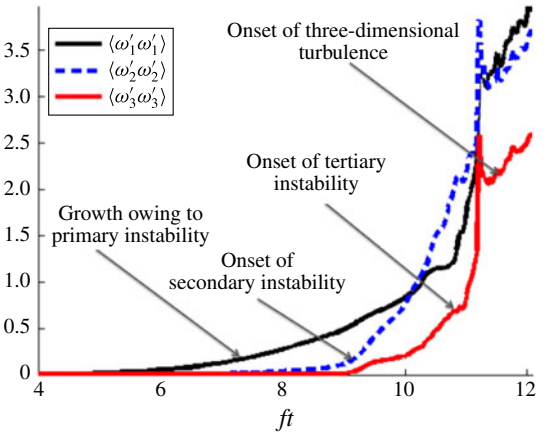


FIGURE 14. (Colour online) Evolution of volume-averaged fluctuating enstrophy components, showing the development of near-SI followed by secondary instabilities and finally three-dimensional turbulence.

6.2. *Quantitative analysis*

The nonlinear breakdown to turbulence is rather rapid and proceeds through a three-step process, as was explained in § 6.1. This picture is reinforced quantitatively by figure 14, which shows the evolution of volume-averaged vorticity fluctuations broken down by component. From this plot, times with qualitative changes in vorticity fluctuations can be identified. When $ft \sim 9$, the rate of change of $\omega_2'^2$ and $\omega_3'^2$ rapidly increases, corresponding to the emergence of the secondary shear-convective instability. Next, when $ft \sim 11$, the rate of change of $\omega_1'^2$ and $\omega_3'^2$ rapidly increases due to tertiary instability. Lastly, when $ft \sim 11.2$, enstrophy shows a sudden decrease followed immediately by growth. It is after $ft \sim 11.2$ that the domain fills with small-scale vortical fluctuations and the entire flow becomes turbulent. These results reinforce the notion of three discrete transitional events in the flow which were evident from the instantaneous snapshots of vorticity.

The bulk energetics of the flow are given via turbulent kinetic (introduced in § 5.2) and potential energy budgets in figure 15, with potential energy budget terms defined as

$$P_\rho = \langle \rho' u_2' \rangle, \quad -B = -\beta \langle \rho' u_3' \rangle \quad \text{and} \quad \epsilon_\rho = \frac{Ek}{Pr} \left\langle \frac{\partial \rho'}{\partial x_i} \frac{\partial \rho'}{\partial x_i} \right\rangle . \tag{6.1a–c}$$

The turbulent kinetic energy budget shows discrete events at $ft \sim 9$ when shear production (P) switches on as a source, $ft \sim 11$ when buoyancy flux (B) switches sign to become a sink, and $ft = 11.2$ when dissipation suddenly jumps. All three are consistent with the observed vorticity dynamics, with P switching on due to the onset of secondary shear-convective instability, B switching off due to the development of three-dimensionality through tertiary instability and dissipation peaking when the three-dimensional fluctuations develop into small-scale turbulence that fills the domain. The turbulent potential energy budget shows the rate of extraction of energy from potential energy in the front (P_ρ), the negative buoyancy flux ($-B$) and potential energy dissipation (ϵ_ρ). Here, P_ρ shows a drop following secondary instability and

https://doi.org/10.1017/jfm.2015.564 Published online by Cambridge University Press

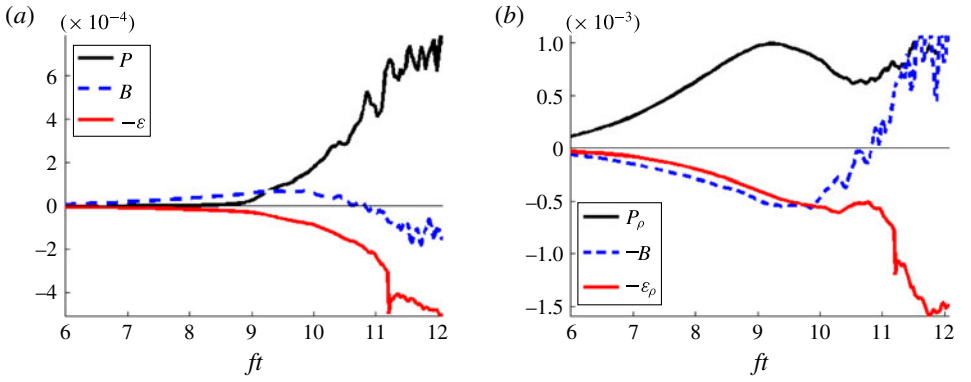


FIGURE 15. (Colour online) Terms from the volume-averaged turbulent kinetic energy (*a*) and turbulent potential energy (*b*) budgets throughout the duration of case Turb10.

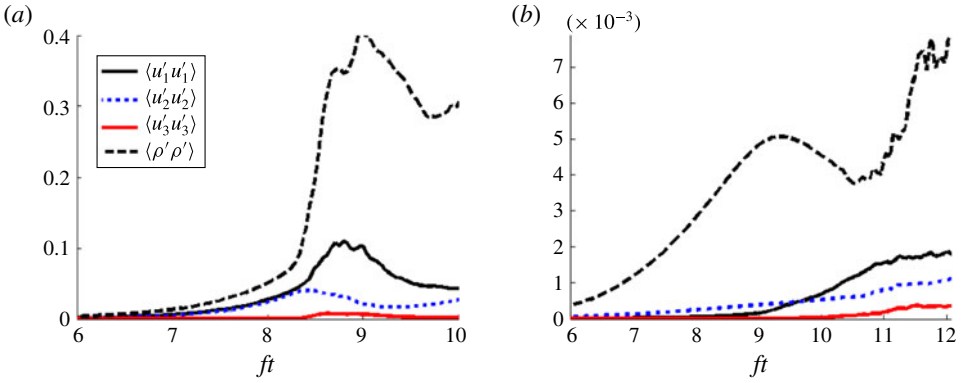


FIGURE 16. (Colour online) Volume-averaged energetics throughout the duration of cases 2D0 (*a*) and Turb10 (*b*).

dissipation shows a dramatic ramp-up after the tertiary instability and increases further once the flow is turbulent. The mixing efficiency can be approximated by the ratio of time-integrated ϵ_ρ to time-integrated P_ρ. The turbulent potential energy budget suggests very high mixing efficiency under this definition, and it appears that very efficient mixing would continue in the turbulent regime. Comparing the magnitudes of ϵ_ρ and $\epsilon + \epsilon_\rho$ also suggests a high mixing efficiency, taking values of roughly 75 % in the turbulent regime.

Figure 16 shows the evolution of turbulence energetics in cases 2D0 and Turb10. A much larger proportion of energy is contained within the density fluctuations early in the evolution of Turb10. This is consistent with the misalignment of near-symmetric currents extracting available potential energy from the front. A reduction in $\langle \rho' \rho' \rangle$ is observed during the period of shear-convective secondary instability when $9 \lesssim ft \lesssim 11$. The amplitude of vertical velocity fluctuations relative to the horizontal fluctuations in the three-dimensional case is not nearly as small as in the two-dimensional case. It is also worth noting that the two-dimensional case develops unrealistically large fluctuation amplitudes compared with the three-dimensional turbulent case.

https://doi.org/10.1017/jfm.2015.564 Published online by Cambridge University Press

7. Conclusion

This study explores the development of instability and turbulence in a symmetrically unstable variant of Eady's model with $Ri = 0.5$. The novelty of the approach is the simulation of fully three-dimensional turbulence in a baroclinic flow with boundaries that is unstable to symmetric instability. The flow progresses through a sequence of instabilities whose effect is quantified, e.g. the temporal evolution of volume-averaged vorticity fluctuations in figure 14. Linear stability analysis is also performed to understand and interpret three-dimensional effects which are manifested not only in transition to turbulence but also during the initial evolution of small-amplitude three-dimensional disturbances.

The initial vertical vorticity fluctuations organize into structures that are inclined at approximately -45° in the x_1–x_2 plane and instability currents that are misaligned with respect to the isopycnals. This behaviour for $ft = O(1)$ is consistent with the results of Mamatsashvili *et al.* (2010). As time advances, the horizontal scale of the flow continually increases, especially in the along-front direction, and the flow tends towards two-dimensionality. However, for sufficiently large horizontal domains, nonlinearity emerges for currents that, although near-symmetric (the angle θ between the current and the symmetric axis is roughly 5° in the largest-domain case), are not exactly symmetric. In other words, it is the asymmetric instability that evolves nonlinearly rather than the purely symmetric ($k_1 = 0$) instability. The sensitivity of this finding of nonlinearly evolving asymmetric instability to the choice of initial conditions for the fluctuations (the horizontal length scale is larger than the vertical length scale in the present case, as in geophysical flows) and the Reynolds number is worth exploring in future three-dimensional studies.

Non-modal linear stability analysis showed a tendency for the flow to nearly align with the symmetric axis once $ft \gg 1$ for strong shear ($|S/f| \gg 1$) and stratification ($|N/f| \gg 1$). The vertical scale of the observed asymmetric modes decreases with time, resulting in misalignment of asymmetric currents and isopycnals. The analysis shows that vertical shear stabilizes nearly symmetric modes tilted in the direction opposite to that observed in the simulations, explaining why the oppositely tilted modes do not amplify in the simulations. For these modes, k_3/k_2 decreases in magnitude with time, leading to currents that are steeper than the isopycnal slope, resulting in rapid suppression. It is because of these issues that the analysis of purely symmetric instability through two-dimensional simulations may not be appropriate for frontal zones with strong lateral density gradients and vertical shear.

The computational domains are rotated about the vertical axis to investigate near-symmetric currents in both the linear stability analysis and numerical simulations. A two-dimensional simulation rotated to be nearly aligned with the 5° asymmetric currents found in the three-dimensional direct numerical simulation displayed perturbation growth rates similar to those seen in the three-dimensional simulation. Misalignment of asymmetric currents and isopycnals allows currents to be strengthened by both the reservoir of kinetic energy in the vertical shear and the reservoir of potential energy in the density front, simultaneously. The secondary shear instability is misaligned with the symmetric axis, implying that two-dimensional simulations are unable to accurately capture secondary shear instabilities in both symmetric and asymmetric currents.

Finally, the forward cascade from balanced vertical shear to turbulence is demonstrated using a high-resolution simulation with the computational domain rotated about the vertical axis by 10°. The quiescent flow develops a primary instability that takes the form of nearly two-dimensional asymmetric currents.

https://doi.org/10.1017/jfm.2015.564 Published online by Cambridge University Press

When the perturbations become large during the transient growth period, there is a secondary (originating in the y–z plane where y is the cross-front direction and z is vertical) shear-convective instability. Another important transition event related to a tertiary instability (see figure 14) occurs later, and is not present in two-dimensional simulations. The balanced base flow has mean shear flow, $\langle u_1 \rangle(x_3)$, that is stable to ω_2 fluctuations for $Ri = 0.5$. During the tertiary instability, lateral vorticity fluctuations (ω_2') grow large enough for nonlinearity to overcome the organization of the balanced base flow, enhancing extraction of kinetic energy from the shear. This transition leads to fully three-dimensional vortical flow which rapidly becomes more multiscale until three-dimensional well-developed shear-driven turbulence emerges. The mixing of the density field (ϵ_ρ) is strong and increases by a factor of three after the destabilization of the shearing plane, which is also not present in two-dimensional simulations.

Acknowledgements

The authors are grateful for computational resources through a research allocation through the Extreme Science and Engineering Discovery Environment (XSEDE) and for the detailed helpful comments of the reviewers.

REFERENCES

D'Asaro, E., Lee, C., Rainville, L., Harcourt, R. & Thomas, L. 2011 Enhanced turbulence and energy dissipation at ocean fronts. *Science* **332** (6027), 318–322.

Eady, E. T. 1949 Long waves and cyclone waves. *Tellus* **1**, 33–52.

Griffiths, S. D. 2003*a* The nonlinear evolution of zonally symmetric equatorial inertial instability. *J. Fluid Mech.* **474**, 245–273.

Griffiths, S. D. 2003*b* Nonlinear vertical scale selection in equatorial inertial instability. *J. Atmos. Sci.* **60**, 977–990.

Hoskins, B. 1974 The role of potential vorticity in symmetric stability and instability. *Q. J. R. Meteorol. Soc.* **100**, 480–482.

Jeong, J. & Hussain, F. 1995 On the identification of a vortex. *J. Fluid Mech.* **285**, 69–94.

Jones, S. & Thorpe, A. 1992 The three-dimensional nature of 'symmetric' instability. *Q. J. R. Meteorol. Soc.* **118**, 227–258.

Lott, F., Plougonven, R. & Vanneste, J. 2012 Gravity waves generated by sheared three-dimensional potential vorticity anomalies. *J. Atmos. Sci.* **69**, 2134–2151.

Mamatsashvili, G., Vsarlosov, V., Hagelishvili, G., Hanishvili, R. & Kalashnik, M. 2010 Transient dynamics of nonsymmetric perturbations versus symmetric instability in baroclinic zonal shear flows. *J. Atmos. Sci.* **97**, 2972–2989.

Moffatt, H. K. 1967 The interaction of turbulence with strong wind shear. In *Proceedings of the 1965 URSI–IUGG International Colloquium on Atmospheric Turbulence and Radio Wave Propagation* (ed. A. M. Yaglom & V. I. Tatarsky), pp. 139–154. Nauka.

Molemaker, M., McWilliams, J. & Capet, X. 2010 Balanced and unbalanced routes to dissipation in an equilibrated Eady flow. *J. Fluid Mech.* **654**, 35–63.

Pedlosky, J. 1987 *Geophysical Fluid Dynamics*, 2nd edn. Springer.

Pieri, A., Godeferd, F., Cambon, C. & Salhi, A. 2013 Non-geostrophic instabilities of an equilibrium baroclinic state. *J. Fluid Mech.* **734**, 535–566.

Rogallo, R. S. 1981 Numerical experiments in homogeneous turbulence, *NASA Tech. Rep.* 81315.

Salhi, A. & Pieri, A. B. 2014 Wave–vortex mode coupling in neutrally stable baroclinic flows. *Phys. Rev.* E **90**, 1–15.

Stone, P. 1966 On non-geostrophic baroclinic stability. *J. Atmos. Sci.* **23**, 390–400.

Stone, P. 1970 On non-geostrophic baroclinic stability: part ii. *J. Atmos. Sci.* **27**, 721–726.

https://doi.org/10.1017/jfm.2015.564 Published online by Cambridge University Press

TAYLOR, J. & FERRARI, R. 2009 On the equilibrium of a symmetrically unstable front via a secondary shear instability. *J. Fluid Mech.* **622**, 103–113.

THOMAS, L., TAYLOR, J., FERRARI, R. & JOYCE, T. 2013 Symmetric instability in the Gulf Stream. *Deep-Sea Res.* II **91**, 96–110.

THORPE, A. & ROTUNNO, R. 1989 Nonlinear aspects of symmetric instability. *J. Atmos. Sci.* **46**, 1285–1299.

https://doi.org/10.1017/jfm.2015.564 Published online by Cambridge University Press